ACS Catalysis

pubs.acs.org/acscatalysis

Research Article

Single-Step Conversion of Ethanol to *n*-Butene over Ag-ZrO_2/SiO_2 Catalysts

Vanessa Lebarbier Dagle,* Austin D. Winkelman, Nicholas R. Jaegers, Johnny Saavedra-Lopez, Jianzhi Hu, Mark H. Engelhard, Susan E. Habas, Sneha A. Akhade, Libor Kovarik, Vassilliki-Alexandra Glezakou, Roger Rousseau, Yong Wang, and Robert A. Dagle*

Cite This: *ACS Catal.* 2020, 10, 10602−10613

Read Online

ACCESS | Metrics & More | Article Recommendations | Supporting Information

ABSTRACT: Ethanol is a promising platform molecule for production of a variety of fuels and chemicals. Of particular interest is the production of middle distillate fuels (i.e., jet and diesel blendstock) from renewable ethanol feedstock. State-of-the-art alcohol-to-jet technology requires multiple process steps based on the catalytic dehydration of ethanol to ethylene, followed by a multistep oligomerization including *n*-butene formation and then hydrotreatment and distillation. Here we report that, over Ag-ZrO_2/SBA-16 with balanced metal and Lewis acid sites, ethanol is directly converted to *n*-butene (1- and 2-butene mixtures) with an exceptional butene-rich olefin selectivity of 88% at 99% conversion. The need for the ethanol dehydration to ethylene step is eliminated. Thus, it offers the potential for a reduction in the number of required processing units versus conventional alcohol-to-jet technology. We also found that the C_4 product distribution, *n*-butene and/or 1,3-butadiene, can be tailored on this catalyst by tuning the hydrogen feed partial pressure and other process/catalyst parameters. With sufficient hydrogen partial pressure, 1,3-butadiene is completely and selectively hydrogenated to form *n*-butene. The reaction mechanism was elucidated through operando-nuclear magnetic resonance investigations coupled with reactivity measurements. Ethanol is first dehydrogenated to acetaldehyde over the metallic Ag, then acetaldehyde is converted to crotonaldehyde over the acid sites of ZrO_2/SiO_2 via aldol condensation followed by dehydration. This is followed by a Meerwein−Ponndorf−Verley reduction of crotonaldehyde to butadiene intermediate that is hydrogenated into *n*-butene over metallic Ag and ZrO_2. A minor fraction of *n*-butene is also produced from crotonaldehyde reduction to butyraldehyde instead of butadiene. Isotopically labeled ethanol NMR experiments demonstrated that ethanol, rather than H_2, is the source of H for the hydrogenation of crotonaldehyde to butyraldehyde. Combined experimental-computational investigation reveals how changes in silver and zirconium composition and the silver oxidation state affects reactivity under controlled hydrogen partial pressures and after prolonged run times. Finally, catalyst effectiveness also was demonstrated when using wet ethanol feed, thus highlighting process flexibility in terms of feedstock purity requirements.

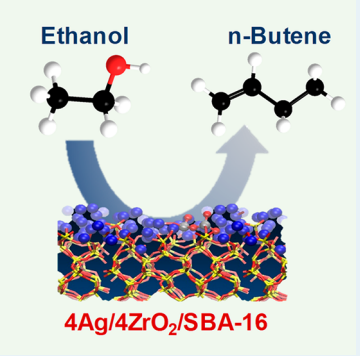

KEYWORDS: *ethanol, n-butene, olefins, single-step, biomass, alcohol-to-jet*

INTRODUCTION

The increasing demand for energy coupled with the depletion of fossil resources and stringent environmental regulations has led to increased interest in alternative and renewable energy resources such as biomass. Ethanol represents a promising platform molecule for the production of fuels and chemicals from renewable resources. Currently, most ethanol is produced by fermenting sugars derived from corn starch or sugar cane. Nonedible cellulosic feedstocks are attractive, because they are widely available, abundant, and relatively inexpensive; however, they currently represent a more costly option for producing ethanol.[1] Ethanol also can be produced by enzymatic or thermocatalytic upgrading of syngas derived from biomass, municipal solid waste, or industrial waste gases (e.g., from steel mills).[2−7] Taken together, the ethanol "blend wall" coupled with advancements in production efficiency and feedstock diversification may potentially lead to excess ethanol at competitive prices available for production of a wide range of fuels and commodity chemicals.[8]

The production of distillate fuel from ethanol is commercially done using the alcohol-to-jet (ATJ) technology. The ATJ process comprises multiple processing steps. Ethanol first undergoes catalytic dehydration to form ethylene, followed by oligomerization over solid acid catalyst(s). Olefins then are hydrogenated to form paraffins followed by fractionation into jet-range blendstock. Ethylene oligomeriza-

Received: May 20, 2020
Revised: July 9, 2020
Published: July 20, 2020

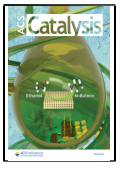

https://dx.doi.org/10.1021/acscatal.0c02235
ACS Catal. 2020, 10, 10602−10613

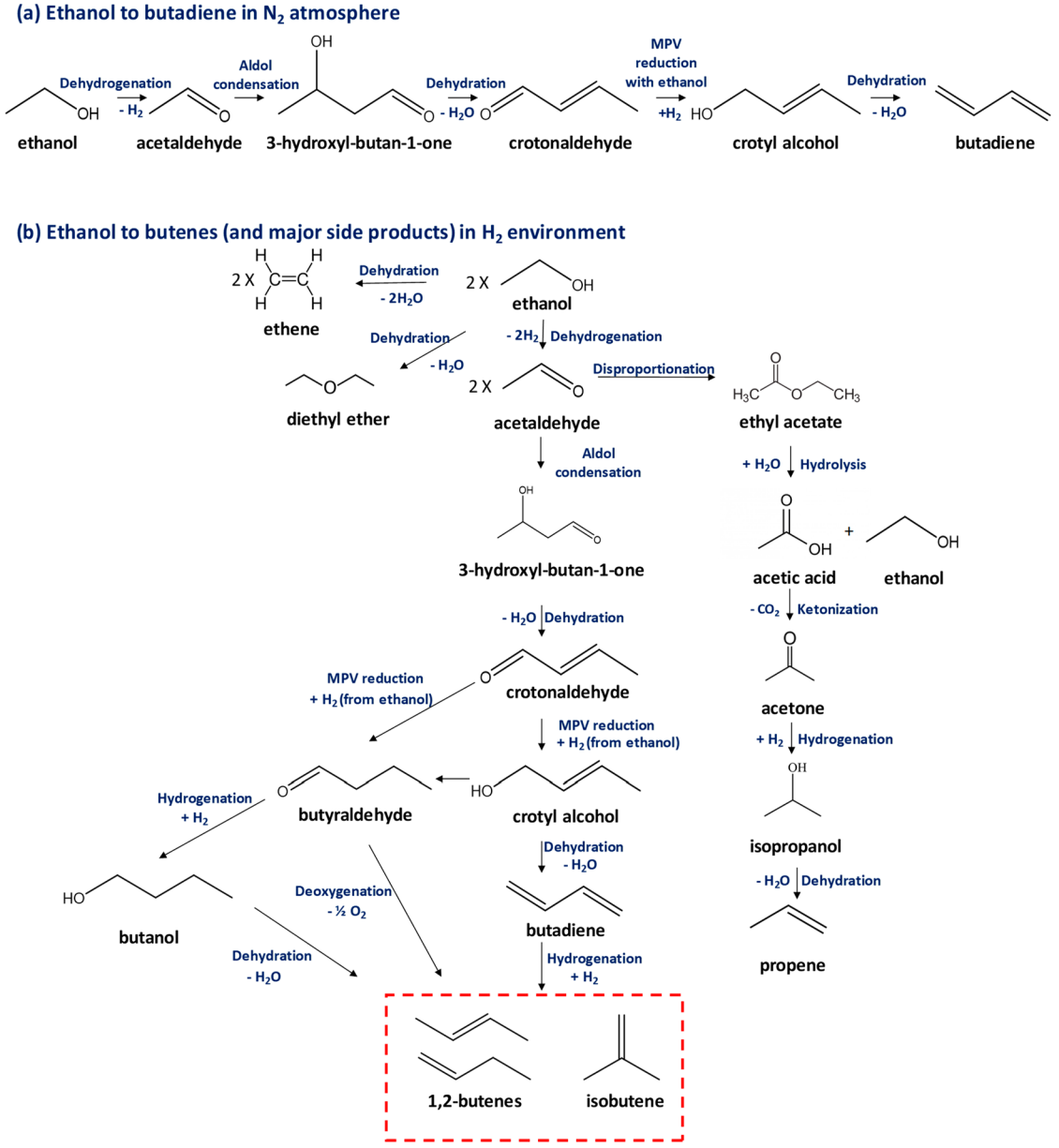

Figure 1. (a) Main reaction pathway for 1,3-butadiene formation from ethanol with N_2 cofeed over Ag-ZrO_2/SBA16. (b) Potential routes for *n*-butene formation and major side products from ethanol with H_2 cofeed over Ag-ZrO_2/SBA-16. Adapted from ref 23.

tion can proceed either in one or two steps.[9−12] Single-step ethylene oligomerization has low selectivity toward fuel-range hydrocarbons because of the high selectivity to undesirable C_1−C_4 light hydrocarbons (∼40%).[13−16] Thus, a two-step ethylene oligomerization process has been reported in which ethylene first is oligomerized to a *n*-butene-rich olefin stream and then oligomerized to jet-range olefins.[11] For example, at Pacific Northwest National Laboratory, we reported a two-step oligomerization process that produces primarily isoparaffinic hydrocarbons forming minimal aromatic compounds, facilitates efficient conversion of high carbon fractions to distillate range fuels, and minimizes formation of naphtha-like compounds by efficient intermediate product recycling.[11,12]

In this paper, we report on a new catalytic route for the direct production of *n*-butene from ethanol over a Ag-ZrO_2/SBA-16 catalyst. Direct ethanol conversion to *n*-butene is advantageous over the current state-of-the-art ATJ process, because it eliminates the ethylene oligomerization step. Thus, it reduces the number of unit operations. Furthermore, it enables some energy savings, because ethanol deoxygenation to ethylene is endothermic, whereas direct conversion of ethanol to *n*-butene is slightly exothermic. However, carbon-efficient processes for direct ethanol conversion to *n*-butene have yet to be reported. Thus, the goal of this study was to selectively produce *n*-butene directly from ethanol. We note that production of isobutylene directly from ethanol was previously demonstrated[17−19] using $Zn_xZr_yO_z$ mixed-oxide-type catalysts. However, the maximal yield toward isobutylene-rich olefins is limited to ∼50 to 60% because of the stoichiometric requirement of CO_2 formation (∼33% CO_2 selectivity) due to the ketonization step in the mechanism. With Ag-ZrO_2/SBA-16 catalyst *n*-butene formation via C−C coupling is achieved via aldol condensation rather than ketonization potentially reaching 100% carbon efficiency,

https://dx.doi.org/10.1021/acscatal.0c02235
ACS Catal. 2020, 10, 10602−10613

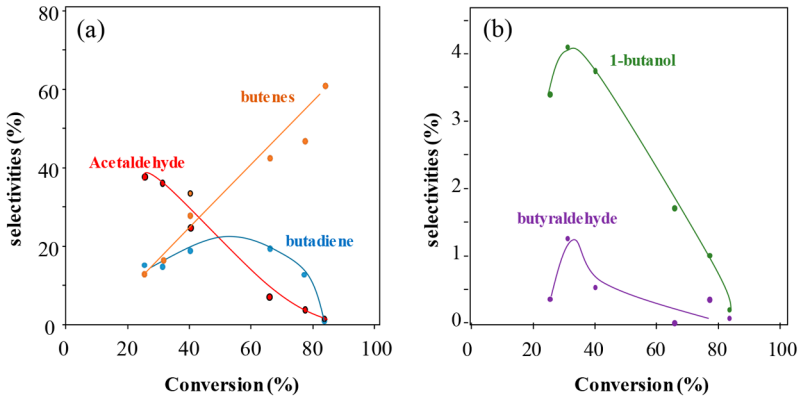

Figure 2. Evolution of the (a) main product selectivities as a function of the conversion and (b) butyraldehyde and 1-butanol selectivities as a function of the conversion over 4Ag-4ZrO_2/SBA-16. T = 325 °C, P = 7 bar, WHSV = 0.2−14.6 h^{-1}, 24 mol % ethanol in N_2. Data collected after 5 h on stream.

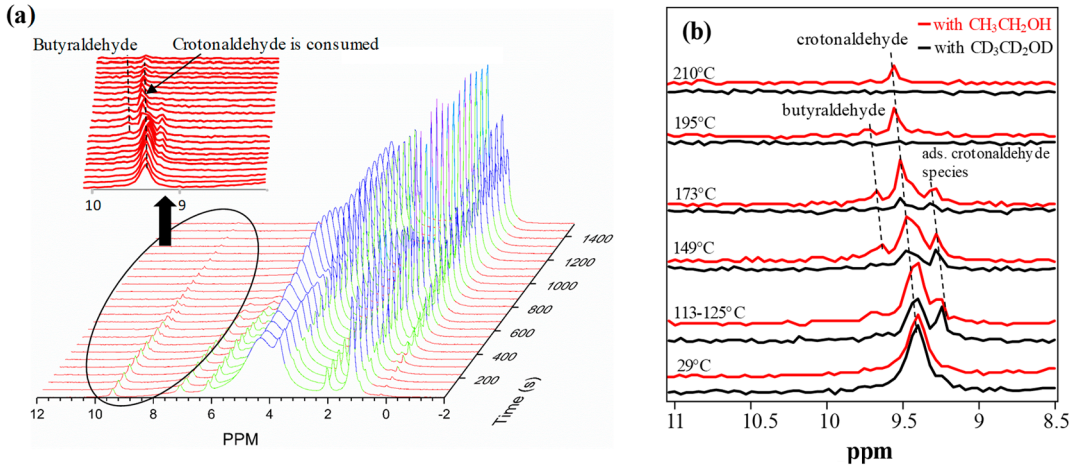

Figure 3. (a) Time-resolved ^{1}H NMR recorded during reaction while ramping from 25 to 210 °C. Feed: ethanol + crotonaldehyde + H_2, 25 mg of 4Ag-4ZrO_2/SBA-16, P = 7 bar. (b) Comparison of the ^{1}H NMR spectra recorded during reaction while ramping from 25 to 210 °C with ethanol + crotonaldehyde + H_2 (red) and deuterated ethanol + crotonaldehyde + H_2 (black) with 4Ag-4ZrO_2/SBA-16, P = 7 bar.

since no carbon is lost as CO_2. In addition, the product distribution between 1,3-butadiene and *n*-butene can be simply modulated by controlling hydrogen (H_2) partial pressure as demonstrated in this study. Furthermore, we show that the process operates efficiently with aqueous ethanol feed enabling flexibility in feedstock requirement. The mechanism for *n*-butene formation from ethanol was elucidated by coupling a reactivity measurement with operando-nuclear magnetic resonance (NMR) techniques. We also present evidence about the oxidation of metallic Ag during reaction leading to a decrease of *n*-butene formation to the benefit of butadiene production.

RESULTS AND DISCUSSION

Reaction Mechanism for Direct Ethanol Conversion to *n*-Butene. Over Ag-ZrO_2/SiO_2 catalysts, ethanol conversion to 1,3-butadiene in an inert (N_2) atmosphere involves ethanol dehydrogenation to acetaldehyde over Ag^0. This is followed by aldol condensation of acetaldehyde into crotonaldehyde over the Lewis acid sites of ZrO_2/SiO_2. Then crotonaldehyde is reduced into butadiene over the Lewis acid sites via a Meerwein-Ponndorf-Verley (MPV) type of reduction with ethanol as the source of H_2 (see Figure 1a).[20,21] We note that we verified the nature of the acid sites (i.e., Lewis acidity) by pyridine and lutidine adsorption/desorption followed by infrared spectroscopy as shown in Figure S1. While operating in a reducing (H_2) atmosphere several pathways can potentially lead to the formation of *n*-butene as shown in Figure 1b. One possibility is that *n*-butene could be obtained through hydrogenation of 1,3-butadiene intermediate over Ag^0 and ZrO_2 as shown in Table S1. The presence of H_2 could also favor the hydrogenation of crotonaldehyde and/or the isomerization of crotyl alcohol into butyraldehyde.[22−25] Then, butyraldehyde could be directly converted into *n*-butene via deoxygenation or hydrogenated to 1-butanol that would undergo dehydration to *n*-butene.[25−27]

A space velocity study was conducted to determine by which pathway(s) *n*-butene is produced. Acetaldehyde, 1,3-butadiene, and *n*-butene were the main products formed as shown in Figure 2a. The selectivity toward acetaldehyde decreases as the conversion increases, suggesting that acetaldehyde is an intermediate involved in the formation of *n*-butene. 1,3-butadiene selectivity increases to 20% at 40−60% conversion and then decreases at higher conversion. This result indicates that 1,3-butadiene is most likely produced from acetaldehyde and that it is further converted to *n*-butene. A small amount of butyraldehyde and 1-butanol were also detected at low

https://dx.doi.org/10.1021/acscatal.0c02235
ACS Catal. 2020, 10, 10602−10613

conversion, as seen in Figure 2b. Their selectivities reach a maximum at ~30% conversion and are equal to 1.3% and 4.1% for butyraldehyde and 1-butanol, respectively. The evolution of butyraldehyde and 1-butanol selectivities with the conversion suggest that both are intermediates involved in the formation of *n*-butene. Considering the respective quantities of 1,3-butadiene, butyraldehyde, and crotonaldehyde over the range of conversions studied, we conclude that *n*-butene is mainly produced via crotonaldehyde reduction to 1,3-butadiene followed by hydrogenation. A small amount of *n*-butene was also produced via crotonaldehyde hydrogenation to butyraldehyde and 1-butanol followed by deoxygenation and/or dehydration.

Since only a small amount of butyraldehyde was detected during the reactivity tests, operando ^{1}H NMR experiments were conducted to confirm the role of butyraldehyde in the formation of *n*-butene. Experiments were conducted with a mixture of ethanol and crotonaldehyde in H_2 and at a total pressure of 7 bar with a small amount of catalyst (i.e., 25 mg) sealed in a rotor to simulate low conversion. Figure 3a presents the ^{1}H NMR spectra recorded during the reaction while increasing the temperature. Resonances characteristic of ethanol (4.7, 3.5, and 1.2 ppm) and crotonaldehyde (9.4, 7.05, and 6.12 ppm) are suppressed during the temperature elevation, as these molecules convert to product and intermediate species. Crotonaldehyde exhibits a transient adsorbed-like species (9.28, 6.3, and 5.8 ppm) at lower temperatures, which dissipates, as a new feature, characteristic of butyraldehyde, develops at ca. 9.7 ppm. The butyraldehyde feature initially intensifies as the temperature increases before decreasing at higher temperatures as it is consumed. Both butyraldehyde and crotonaldehyde shift downfield as the temperature is elevated, indicative of thermal perturbation to the shielding of the proton nuclei in these polar molecules. The shift for crotonaldehyde may also indicate vaporization just above the normal boiling point, given that the shoulder apparently develops at the reaction temperature of ~149 °C (Figure 3b) and replaces the initial peak, illustrating the phase equilibrium between liquid and gaseous chemical species.[28] The consumption of butyraldehyde and the subsequent appearance of peaks characteristic of *n*-butene confirms that butyraldehyde is an intermediate in the formation of *n*-butene. We conducted additional experiments in which ethanol was replaced with deuterated ethanol, and the results are presented alongside the natural abundance analogue in Figure 3b. Surprisingly no feature characteristic of butyraldehyde at 9.7 ppm is detected when operating with deuterated ethanol. This result indicates that the hydrogen needed for the hydrogenation of crotonaldehyde to butyraldehyde originates from ethanol rather than from H_2. It reveals that the mechanism for crotonaldehyde hydrogenation to butyraldehyde follows a Meerwein-Ponndorf-Verley reduction.

To complement this NMR study simulations using ab initio molecular dynamics (AIMD) and density functional theory (DFT) calculations were also performed. The reaction energetics were computed via the MPV mechanism in which crotonaldehyde is reduced in the presence of sacrificial ethanol. Two products via MPV reduction of crotonaldehyde are considered: (1) crotyl alcohol (reducing the aldehyde group [−CHO] of crotonaldehyde to its corresponding alcohol) and (2) butyraldehyde (reducing the carbon double bond (C═C) of crotonaldehyde to its corresponding saturated aldehyde). The former product can be subsequently dehydrated to produce 1,3-butadiene, whereas the latter intermediate can undergo further hydrogenation to form *n*-butene. To investigate the role of H_2 in controlling the reaction selectivity, the Ag-ZrO_2/SiO_2 catalyst models were prepared in the presence and absence of H_2 to simulate equivalent scenarios of a feed containing ethanol/N_2 and ethanol cofed with H_2. We refer the reader to the Supporting Information for comprehensive details of the simulated catalysts and their associated geometric (Figures S2 and S3) and electronic (Figure S4) structures. Table 1 reports the computed energetics of crotonaldehyde reduction on the Ag-ZrO_2/SiO_2 catalyst surface in the absence and presence of adsorbed H_2.

Table 1. Relative Free Energies (ΔG in eV)[a]

$\Delta G_{298\ K}$ (eV)	feed: ethanol	feed: ethanol + H_2
crotonaldehyde → crotyl alcohol	−0.38	1.49
crotonaldehyde → butyraldehyde	−0.18	0.23

[a]Relative free energies computed at 298 K of crotonaldehyde conversion to crotyl alcohol and butyraldehyde via the MPV mechanism on the oxidized Ag-ZrO_2/SiO_2 and reduced Ag-ZrO_2/SiO_2 (via surface adsorbed H species) catalysts. More negative values denote favorable thermodynamic driving force.

Formation of crotyl alcohol via MPV reduction in the absence of H_2 is slightly favorable ($\Delta E_{\text{crotylalcohol | H2-free}} = -0.38$ eV) over butyraldehyde ($\Delta E_{\text{butyraldehyde | H2-free}} = -0.18$ eV). More importantly, in the presence of adsorbed H_2, the reaction energies become significantly unfavorable on the Ag-ZrO_2/SiO_2 catalyst containing surface adsorbed H_2 ($\Delta E_{\text{crotylalcohol | with H2}} = 1.49$ eV and $\Delta E_{\text{butyraldehyde | with H2}} = 0.23$ eV) relative to the H_2-free Ag-ZrO_2/SiO_2 catalyst surface. The DFT-optimized configurations of the reaction intermediates on the Ag-ZrO_2/SiO_2 catalyst surfaces are reported in Figures S5 and S6 of the Supporting Information. The difference in the thermodynamic estimates can be attributed primarily to the altered distribution and oxidation state of Ag (see Figure S4) in the Ag-ZrO_2/SiO_2 catalyst surface due to the presence of hydrogen. Figure S4 shows that the adsorbed H_2 draws out the dispersed interfacial Ag atoms embedded in the SiO_2 matrix (Figure S4a) and alters their oxidation state from $Ag^{\delta+} \rightarrow Ag^0$ as indicated by the evolution of a reduced peak in Figure S4b. This serves to lower the propensity of proton extraction from ethanol ($CH_3-CH_2-O^{\delta-}\cdots H^{\delta+}$) and decrease the thermodynamic driving force to reduce crotonaldehyde. This theoretical analysis both supports and offers explanation for the NMR study finding that the hydrogen required for crotonaldehyde hydrogenation comes from ethanol and not H_2.

Effect of the Process Conditions on Product Distribution. We previously demonstrated how 4Ag-4ZrO_2/SBA-16 is highly effective for converting ethanol into 1,3-butadiene while operating under an inert (N_2) environment and atmospheric pressure.[20] This catalyst system provides the balanced metal and Lewis acid sites required to selectively facilitate a cascading sequence of reactions that includes dehydrogenation, aldol condensation, MPV reduction, dehydration, and hydrogenation. In this report, we show that the process is flexible and can be tuned for the production of *n*-butene instead of 1,3-butadiene under suitable conditions.

Process conditions such as pressure, gaseous environment (N_2 or H_2), and temperature allow modulation of the product slate. As shown in Table 2, while operating at 7 bar and weight

https://dx.doi.org/10.1021/acscatal.0c02235
ACS Catal. 2020, 10, 10602−10613

Table 2. Effect of the Feed Gas Composition on the Reactivity of 4Ag-4ZrO$_2$/SBA-16 for Ethanol Conversion

				selectivity-carbon based (%)									
feed gas	pressure (bar)	WHSV (hr^{-1})	conversion (%)	*n*-butene	butadiene	other olefins[a]	alkanes	diethyl ether	acetaldehyde	butyraldehyde	cyclics[b]	others[c]	total olefins
effect of the feed gas N_2 versus H_2													
N_2	1	0.23	94.2	11.9	67.6	6.5	0.3	1.3	5.9	0.0	0.0	6.5	18.4
N_2	7	0.23	97	23.3	21.1	14.5	1.5	4.2	1.5	0.0	25.5	8.4	37.8
H_2	7	0.23	85.2	51.1	0.4	29.7	2.8	8.4	2.3	1.3	0.0	4.0	80.8
effect of the pressure at similar WHSV and under H_2													
H_2	1	1.4	53.4	8.2	43.8	23.6	0.2	11.3	8.1	2.1	0.1	2.6	31.8
H_2	7	1.4	67.5	27.6	22.3	16.9	1.1	7.7	4.3	17.6	0.9	1.6	41.2
H_2	14	1.4	82.5	28.4	0.0	23.4	11.2	8.2	2.7	3.8	0.0	22.3	51.8
effect of the pressure at similar conversion and under H_2													
H_2	1	0.23	83.4	15.6	59.4	7.9	1.0	9.4	2.9	0.0	0.0	3.8	23.5
H_2	7	0.23	85.2	51.1	0.4	29.7	2.8	8.4	2.3	1.3	0.0	4.0	80.8
H_2	14	1.4	82.5	28.4	0.0	23.4	11.2	8.2	2.7	3.8	0.0	22.3	51.8

[a]Mainly ethylene, propene, and pentenes in the gas phase and C_4^+ olefins in the liquid phase for a run under H_2 at 14 bar. [b]Mainly aromatics, cyclohexanes, and cyclopentanes. [c]Others include mainly oxygenates such as ethyl acetate, 2-ethoxy-butane, diethoxyethane, ethyl ester butanoic acid, acetic acid, methanol, pentanone, and acetone. T = 325 °C, 24 mol % ethanol in N_2 or H_2.

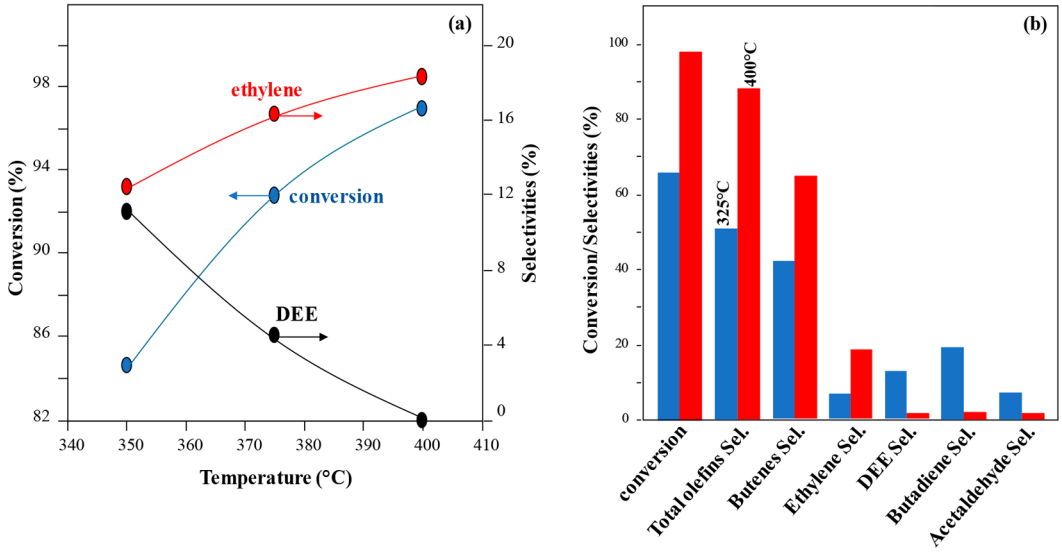

Figure 4. (a) Effect of the reaction temperature on the conversion and selectivity for 4Ag-4ZrO$_2$/SBA-16 at WHSV = 0.91 h^{-1}, P = 7 bar, T = 350–400 °C, 11 mol % ethanol in H_2, TOS = 2 h. (b) Comparison of the conversion and selectivities for 4Ag-4ZrO$_2$/SBA-16 at 325 vs 400 °C for WHSV = 1.4–1.8 h^{-1}, P = 7 bar, 11 mol % ethanol in H_2, TOS = 2 h. T = 325 °C red bars and T = 400 °C blue bars.

hourly space velocity (WHSV) = 0.23 h^{-1}, high selectivity for *n*-butene-rich olefins (i.e., 80.8%) was obtained under an H_2 environment as compared to only 37.8% when operating under an N_2 environment. The low *n*-butene formation under an inert atmosphere is offset by higher formation of 1,3-butadiene and cyclic products. The highest selectivity to 1,3-butadiene (i.e., 63.7%) was obtained while operating under N_2 at atmospheric pressure. Under an H_2 environment, the product distribution is considerably impacted by the pressure. Increasing the pressure from 1 to 14 bar leads to an increase of the *n*-butene-rich olefin selectivity from 31.8 to 51.8%, which is offset by a significant decrease of the 1,3-butadiene selectivity from 43.8 to 0%. However, at a similar conversion from 82.5 to 85.2%, the *n*-butene-rich olefin selectivity (i.e., 80.8%) is the highest when operating at 7 bar. For conversion of ethanol to 1,3-butadiene and *n*-butene-rich olefins over Ag/ZrO$_2$/SiO$_2$ catalysts, ethanol dehydration to ethylene and diethyl-ether (DEE) is a side reaction. Although an ethylene product is less desirable than an *n*-butene product due to the lower carbon number, it is preferred over DEE. For the ethanol dehydration reaction, the ethylene/DEE ratio increases with the reaction temperature.[29] This suggests that it might be beneficial to operate at a higher temperature to eliminate the DEE. The temperature of the ethanol to *n*-butene-rich olefins reaction was thus progressively increased while monitoring the ethylene and DEE formation.

As shown in Figure 4a, DEE formation decreases as the temperature increases, which is beneficial to the formation of ethylene. At 400 °C, no DEE was detected under the present conditions. Figure 4b presents the conversion and product selectivities obtained with 4Ag-4ZrO$_2$/SBA-16 while operating at 325 °C (baseline reaction temperature) and 400 °C. The desired total olefins selectivity is equal to 88% at 400 °C and is 73% higher than that at 325 °C. This is attributed to the increased ethylene/DEE ratio as well as the increased 1,3-butadiene hydrogenation to *n*-butene. Hence, an optimal *n*-butene-rich olefin selectivity of 88% was obtained at 99%

https://dx.doi.org/10.1021/acscatal.0c02235
ACS Catal. 2020, 10, 10602–10613

Table 3. Effect of the Addition of H_2O to the Feed on the Reactivity of 4Ag-4ZrO_2/SBA-16 for Ethanol Conversion to *n*-Butene and Side Products in the Presence of H_2[a]

		selectivity (mol C %)									
feed composition	conversion (%)	ethene	*n*-butene	other olefins[b]	butadiene	alkanes	diethyl ether	acetaldehyde	butyraldehyde	acetic acid	other oxygenates[c]
100 wt % ethanol[d]	93.9	25.7	57.7	3.0	0	6.5	6.0	0.4	0.1	0.7	0.3
95 wt % ethanol/5 wt % H_2O	93.9	19.4	56.9	2.3	0	12.9	6.1	0.3	0.1	0.5	2.2
35 wt % ethanol/65 wt % H_2O	76.4	8.8	54.8	3.6	0	2.1	2.8	6.5	2.3	11.8	8.8

[a]T = 325 °C, P = 7 bar, WHSV = 0.23 h^{-1}, 11 mol % ethanol in H_2 + H_2O, time-on-stream (TOS) = 5 h. [b]Primarily propene and pentenes. [c]Methanol, propanol, butanol, 2-butanone, pentanone, crotonaldehyde, ethyl acetate, and CO_2. [d]Water produced = 2.53 sccm for 8.91 sccm product (carbon-based) equivalent to 41.4 wt % H_2O/58.6 wt % ethanol.

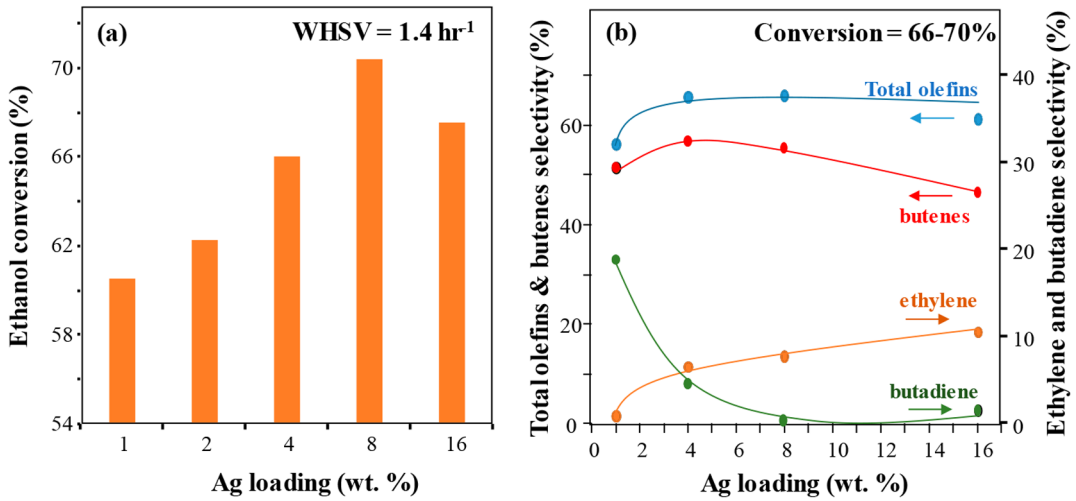

Figure 5. (a) Effect of the Ag loading on the ethanol conversion at WHSV = 1.4 h^{-1}. (b) Selectivity to 1,3-butadiene, *n*-butene (marked here as "butenes"), and total olefins at 66−70% conversion. 4Ag-4ZrO_2/SBA-16 catalysts, T = 325 °C, P = 7 bar, 24 mol % ethanol in H_2, TOS = 5 h.

conversion while operating under H_2 at 7 bar of pressure and a reaction temperature of 400 °C.

Effect of the Addition of H_2O to the Feed on the Catalytic Performance in the Presence of H_2. Ethanol from fermentation broth can be concentrated in water (~40−70 g of ethanol per liter) depending on the purification steps involved.[30] The ability to operate with wet ethanol feeds offers more flexibility and greater applications with potentially lower operating costs. We evaluated the effect of water on reactivity for several water concentrations, and the results obtained are presented in Table 3. The presence of a small amount of water (i.e., 5 wt % H_2O/95 wt % ethanol) in the feed has a negligible effect on both conversion (~94%) and selectivity. When the feed is highly concentrated in water (65 wt % H_2O/35 wt % ethanol) the conversion is lower and equal to ~76%. The loss of conversion is not substantial with small amounts in the feed, which affirms the potential to operate with wet feeds, such as at the azeotropic composition of ethanol and water (i.e., 96 wt %). However, the conversion is markedly lower with more diluted feed. Further, while selectivity to *n*-butene specifically is not negatively impacted, other product selectivities are affected with the presence of water in the feed. For example, oxygenate formation is enhanced with high-water feed concentration (i.e., 65 wt %). Acetic acid formation is especially enhanced, and its selectivity increased to 11.8%. This is likely due to hydrolysis reactions being facilitated in the presence of water.[23] The increase of acetaldehyde selectivity to 6.5% suggests that the presence of water restrains the conversion of acetaldehyde to a 1,3-butadiene intermediate.

The effect of water in the feed on catalytic performance can be rationalized due to the shift in equilibrium that occurs for the many competing reactions in the reaction network (see Figure 1). Specifically, the formation of the initial dehydration side products ethylene and DEE is inhibited. This is illustrated in Table 3, which shows ethylene and DEE contents to decrease with increasing water content in the feed. While selectivities toward the initial dehydration side products are reduced, the competing route to acetaldehyde via dehydrogenation is enhanced, thus in turns facilitating the competing acetaldehyde disproportionation reaction to ethyl acetate and its subsequent hydrolysis to acetic acid. As shown in Table 3, the selectivity toward acetic acid (and other oxygenates) increases with increasing water content. However, aldol condensation of acetaldehyde and its subsequent dehydration is hindered due to the presence of water in the feed, and this affects overall equilibrium conversion to *n*-butene. The end result is a decrease in overall conversion due to a shift in the reaction equilibrium, primarily due to the presence of water, which inhibits dehydration reactions. Further, there is a shift toward products that is facilitated with a water cofeed (e.g., such as acetic acid, which requires hydrolysis). We note that, while here we have *qualitatively* rationalized the conversion and product selectivity, a more detailed kinetic study is required to make *quantitative* comparisons for the different reactions in the reaction network. We also note how we previously

https://dx.doi.org/10.1021/acscatal.0c02235
ACS Catal. 2020, 10, 10602−10613

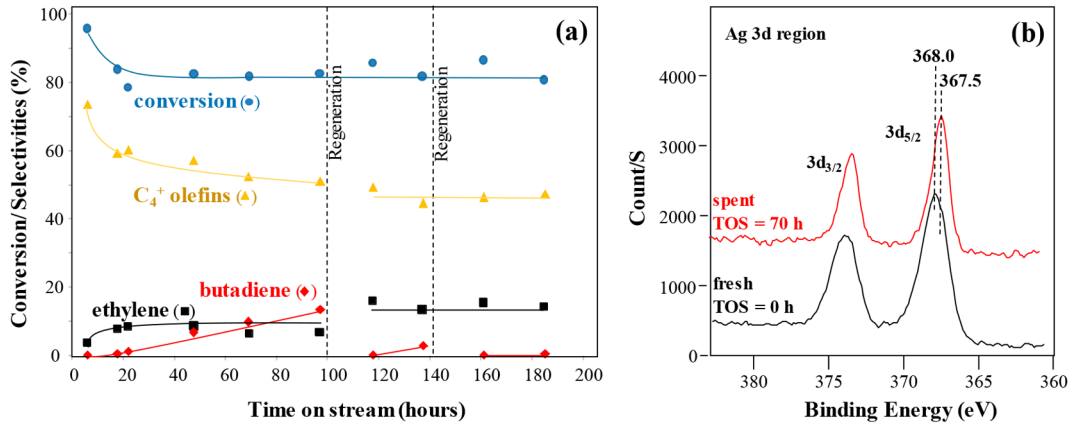

Figure 6. (a) Catalyst lifetime evaluation for 4Ag-4ZrO_2/SBA-16. T = 325 °C, WHSV = 0.23 h^{-1}, P = 7 bar, 24 mol % ethanol in H_2. Regeneration protocol: treatment under 5 mol % O_2/N_2 at 500 °C for 4 h, then decrease temperature to 325 °C under N_2, then treatment under 10 mol % H_2/N_2 for 1 h. (b) XPS results for 4Ag-4ZrO_2/SBA-16 after reduction at 325 °C under 10 mol % H_2/N_2 for 1 h and after 70 h on stream. The reduced and spent 4Ag-4ZrO_2/SBA-16 samples were carefully transferred from the reactor to the XPS chamber without exposure to air.

demonstrated that the conversion of acetaldehyde to 1,3-butadiene occurs over the Lewis acid sites of Ag-ZrO_2/SiO_2 catalysts.[20] In the presence of water, it is possible that some Lewis acid sites are converted into Brønsted-like acid sites, resulting in a decreased acetaldehyde conversion.[31−36] Furthermore, these measurements were conducted after only 5 h on stream, and longer exposure to the wet feed could have greater impact on oxygenate selectivity, which would potentially impact the selectivity of *n*-butene. Taken together, both a shift in reaction equilibrium as well as possible changes to the catalyst active sites could explain how the water cofeed affects the catalytic performance.

Effect of the Catalyst Composition on the Catalytic Performance. We tested a series of Ag-4ZrO_2/SBA-16 catalysts with Ag loadings varying from 1 to 16 wt % for ethanol conversion in the presence of H_2 as shown in Figure 5. While the conversion increases from 60 to 70% with the increase in Ag loading from 1 to 8 wt %, a slight loss of conversion is observed at 16 wt % loading. For Ag > 8 wt %, increasing the Ag loading most likely leads to an increase of the Ag particle sizes rather than an increase of the concentration of active Ag sites resulting in a decrease of conversion. At similar conversion of 66−70%, the product selectivity varies greatly with the Ag loading as reported in Figure 5b. The 1,3-butadiene selectivity decreases drastically from ∼27 to 0% with the increase of Ag loading from 1 to 8 wt %. As the Ag loading increases, ethanol conversion to ethylene is favored, and ethanol conversion to the acetaldehyde intermediate to 1.3-butadiene is restrained. This is attributed to the increase of the Ag particle size with the Ag loading. Indeed, in our previous study theoretical calculations coupled with experimental measurements have shown that less-dispersed Ag promotes the conversion of ethylene to the detriment of butadiene formation.[37] The catalyst with 8 wt % Ag appears promising for the production of *n*-butene-rich olefins, because it presents the highest olefin selectivity of ∼66% with no detectable 1,3-butadiene formation. Separation of *n*-butene from 1,3-butadiene is difficult because of their similar boiling points, and it is preferable to not produce 1,3-butadiene when *n*-butene is the desired product.

Catalyst Lifetime Study. The catalytic performance of 4Ag-4ZrO_2/SBA-16 was evaluated for 180 h on stream, and the results are shown in Figure 6a. An initial decrease of the conversion from ∼98 to ∼82% is observed, but for time-on-stream (TOS) > 20 h minor change in conversion is noticed. The initial drop in conversion could be due to sintering of the Ag^0 particles from ∼3 nm (TOS = 0 h) to 4 nm (TOS = 180 h) as revealed by X-ray diffraction (XRD) (Figure S7). Note that the XRD patterns do not show peaks characteristic of crystalline ZrO_2 in agreement with our transmission electron microscopy (TEM) findings, indicating the presence of amorphous ZrO_x patches Figure S8. The selectivity to C_4^+ olefins decreases with TOS to the benefit of the 1,3-butadiene selectivity. We believe that the interchange in selectivities is related to a gradual oxidation of Ag^0 particles during reaction due to the water produced from the dehydration steps. Indeed, separate results from X-ray photoelectron spectroscopy (XPS) experiments conducted on the reduced and spent catalysts (see Figure 6b) show a decrease of the binding energy after exposure to reaction. This is indicative of a higher oxidation state of Ag for the spent sample. Hence, it is possible that the number of Ag^0 particles active for 1,3-butadiene hydrogenation to *n*-butene decreases during reaction due to an increase of the number of oxidized Ag particles. We conducted a regeneration treatment consisting of an oxidation for coke removal followed by reduction to allow Ag^0. After regeneration of the catalyst, 1,3-butadiene formation was suppressed, thus confirming that the progressive decrease of *n*-butene formation during reaction was due to a partial oxidation of Ag^0. Ethylene production increased after regeneration, but this finding is not fully understood yet. We note that the Raman spectra obtained for the spent catalyst (see Figure 7) indicates the presence of coke, with bands at 1597 and 1360 cm^{-1} corresponding to the G band and the D band, respectively, of the graphitic carbon species, suggesting that operating for longer TOSs would result in a reversible loss of conversion.

Benefits of the Process. In the present study we demonstrated carbon-efficient conversion of ethanol to *n*-butene in a single step over Ag-ZrO_2/SBA-16 catalysts. An exceptional *n*-butene selectivity of 65% at 98% conversion was obtained while operating at 400 °C corresponding to a productivity of 3.22 g of butenes per gram of catalyst per hour. As shown in Table 4 below, this represents a significant advancement compared to the state-of-the-art, since the highest *n*-butene selectivity reported before was equal to 26.7% at full conversion and over Sc(3)/In_2O_3. Direct

https://dx.doi.org/10.1021/acscatal.0c02235
ACS Catal. 2020, 10, 10602−10613

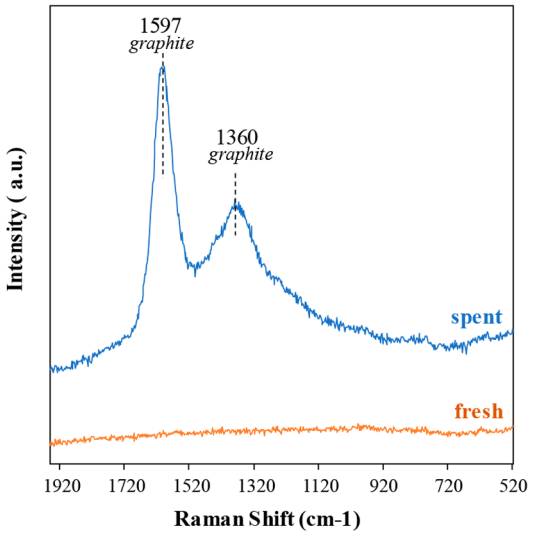

Figure 7. Raman spectra recorded between 520 and 1935 cm^{-1} for 4Ag-4ZrO_2/SBA-16 before (fresh) and after (spent) reaction shown in Figure 6a.

Table 4. Catalytic Performance Comparison between This Work and the Best-Performing Catalysts from the Literature for Direct Conversion of Ethanol to Olefins using Fixed-Bed Reactors[16,17,37−42]

catalyst	temperature (°C)	conversion (%)	*n*-butene selectivity (%) (carbon-based)	refs
4Ag-4ZrO_2/SBA-16	375	93	66	this study
	400	98	65	
$Zn_1Zr_{10}O_x$	450	>99	42[a]	17,18
Sc(3)/In_2O_3	500	100	26.7	38
Ce-HZSM5	400	100	20	39
Fe−H-ZSM5	400	91.5	18.2	40
H-ZSM5	375	100	15.7	41
Ni-MCM41	350	100	8.1	42,43

[a]The product is isobutylene instead of linear *n*-butene.

conversion of ethanol to isobutylene was also reported before, and an isobutylene selectivity of 42% (at greater than 99% conversion) was obtained with $Zn_1Zr_{10}O_x$.

Butenes are distillate fuel precursors. As explained earlier, the ATJ process converts ethanol to ethylene via dehydration, then ethylene is oligomerized to *n*-butene, and this is followed by oligomerization and hydrogenation to paraffins and fractionation into jet-range blendstock. Compared to the ATJ process this new process presents several advantages. First, ethanol is directly converted into *n*-butene, which decreases the number of unit operations potentially enabling lower capital investment. In addition, the ethanol deoxygenation to ethylene and ethylene C−C coupling to form *n*-butene are combined in one single step that is slightly exothermic. This translates into energy savings compared to the ATJ process, where the ethanol dehydration to ethylene is endothermic. Then, as demonstrated in this study, this process appears compatible with aqueous ethanol offering some flexibility in terms of feedstock requirement. Finally, the multifunctional Ag-ZrO_2/SBA-16 catalyst allows a coproduct option with butadiene offering a market strategy flexibility to the process.

CONCLUSION

In conclusion, we report a new process whereby a multifunctional Ag-ZrO_2/SBA-16 catalyst can facilitate direct conversion of ethanol to *n*-butene. We achieved an 88% butene-rich olefin selectivity at almost full conversion. Mechanistically, we determined how *n*-butene is formed primarily from the reduction of crotonaldehyde to form 1,3-butadiene followed by selective hydrogenation. A small fraction of *n*-butene is produced from butyraldehyde hydrogenation with ethanol, as confirmed by operando NMR experiments coupled with theoretical insights. While operating with a wet ethanol feed (e.g., 35 wt % ethanol/H_2O), no significant change in *n*-butene production was observed. A catalyst lifetime study revealed that a decrease in *n*-butene olefin selectivity corresponded with an increase in 1,3-butadiene selectivity with TOS, which we attributed to the progressive oxidation of Ag^0.

MATERIALS AND METHODS

Catalysts Preparation. A series of xAg-4ZrO_2/SiO_2 catalysts were synthesized by incipient wetness impregnation of SiO_2 (SBA-16, ACS Materials) with silver nitrate powder and zirconyl nitrate solution dissolved in deionized water. After impregnation, the catalysts were dried at 110 °C for 8 h and calcined at 500 °C for 4 h. We varied the Ag loading "x" from 1 to 16 wt %.

Reactivity Measurements. Reactivity tests for the conversion of ethanol to 1,3-butadiene were conducted in a 6.35 mm outer diameter (inner diameter = 4.57 mm) fixed-bed, packed-bed reactor loaded with 2.0 g of catalyst. A K-type thermocouple was placed in the reactor to measure the catalyst bed temperature. To minimize temperature gradients, an electrical resistance heating block was installed on the reactor. Prior to testing, catalysts were first activated in situ at 450 °C for 8 h under 120 SCCM of N_2. Then, the temperature was cooled to 325 °C, and the catalysts were reduced under 100 SCCM of 10 mol % H_2/N_2 for 1 h. Then, the pressure was increased to 7 bar under 50 sccm H_2. Ethanol fed into the system using an ISCO syringe pump was converted to the gas phase using a vaporizer consisting of 6.6 mm inner diameter steel tubing filled with quartz beads. The effects of conversion and selectivity were measured at 325 °C, at varied pressure and at varied WHSV as noted. Either N_2 or H_2 typically was used as the carrier gas. A knockout pot placed directly downstream of the reaction zone was used to collect liquid product. Gaseous effluent was analyzed online using an Inficon micro-GC (model 3000A) equipped with MS-5A, Plot U, alumina, OV-1 columns, and a thermal conductivity detector. Liquid samples collected from the knockout pot were analyzed separately ex situ using liquid chromatography. The ethanol conversion and the product selectivities were calculated as presented in equations [1] and [2] below. The carbon balance was typically within 10%.

$$\text{ethanol conversion (\%)} = \frac{100 \times (\text{moles ethanol})\text{in} - (\text{moles ethanol})\text{out}}{(\text{moles ethanol})\text{in}} \quad (1)$$

$$\text{carbon selectivity product } i \text{ (\%)} = \frac{100 \times \text{moles of carbon in product } i}{\text{total carbon moles in identified products}} \quad (2)$$

https://dx.doi.org/10.1021/acscatal.0c02235
ACS Catal. 2020, 10, 10602−10613

Catalyst Characterization. XPS Spectra were collected using a Physical Electronics Quantera Scanning X-ray Microprobe. This system uses a focused monochromatic Al Kα X-ray (1486.7 eV) source for excitation and a spherical section analyzer. The X-ray beam is incident normal to the sample, and the photoelectron detector is at 45° off normal. High-energy resolution spectra were collected using a pass energy of 69.0 eV with a step size of 0.125 eV. The X-ray beam diameter was ~100 mm and was scanned over a 1000 mm × 200 mm area of the sample. For the Ag $3d_{5/2}$ line, these conditions produced a full width at half-maximum value of 0.92 ± 0.05 eV. The binding energy scale was calibrated using the Cu $2p_{3/2}$ feature at 932.62 ± 0.05 eV and the Au $4f_{7/2}$ feature at 83.96 ± 0.05 eV. Some samples experienced variable degrees of charging. Low-energy electrons at ~1 eV, 20 μA and low-energy Ar^+ ions were used to minimize this charging. Charge correction was performed by referencing the Si 2p line to 103.5 eV. The spent catalysts were carefully transferred from the reactor to the XPS glovebox to avoid exposure to air.

The NMR spectra were collected with a 300 MHz Varian Inova NMR spectrometer operating at a ^{1}H Larmor frequency of 299.97 MHz. Samples were spun at the magic angle at 4500 Hz in a commercial 7.5 mm ceramic probe. A single-pulse width of 5 μs and a recycle delay time of 0.5 s were used to collect 128 accumulations per spectrum, corresponding to a temporal resolution of 64 s. The experimental temperature was controlled using a commercial variable-temperature heating stack, externally calibrated with an ethylene glycol thermometer. The sample heating rate was ~10 °C/min. All free indication decays were processed without line broadening, and data were baseline-subtracted to negate probe background. Samples were prepared ex situ in a drybox and charged with the desired quantity of liquid and gaseous substrates prior to sealing into the high-temperature, high-pressure NMR rotor system.

Raman spectra were collected using a Horiba Jobin-Yvon LabRAM HR800 confocal Raman system with a He−Cd laser (Kimmon IK5751I-G) with a wavelength of 325 nm and an output intensity of 30 mW as the excitation source. The laser was directed through a 400 μm confocal hole and focused onto the sample through a 15x-NUV objective. Backscattered light was collected through the same objective and directed to a spectrometer equipped with a charge-coupled device (CCD) detector. To minimize sample degradation, two accumulations of 16 s were acquired for all spectra, and additional laser exposure was minimized. Spectra were collected from 200 to 1800 cm^{-1}.

Computational Methods. We refer the reader to the Supporting Information for a comprehensive description of the construction and model details of the $Ag/ZrO_2/SiO_2$ catalyst model employed in this study. The catalyst model was adapted from our previous study that examines the role of Ag dispersion on the selective conversion of ethanol to butadiene versus ethylene.[37] Choices regarding the size, simulated temperature treatment, proximity, and distribution of the Ag, ZrO_2, and SiO_2 constituents in the catalyst model were based on our recent results obtained from the TEM characterization of the $4Ag\text{-}4ZrO_2/SBA\text{-}16$ catalyst.[37] DFT calculations based on the AIMD simulations were conducted with the Perdew, Burke, and Ernzerhof[44] exchange-correlation functional of the generalized gradient approximation as implemented in the CP2K package.[45] The core electrons were formulated with the Goedecker−Teter−Hutter pseudopotentials,[46] and the valence wave functions were expanded using double-ζ Gaussian basis sets to minimize linear dependence and superposition errors.[47] A plane-wave basis set was employed for all calculations with a cutoff of 400 Ry. The Brillouin zone was integrated using a Γ-point approximation. Dispersion corrections were implemented using Grimme's third-generation DFT-D3 approach.[48]

To obtain a well-equilibrated catalyst model that could provide reliable reactivity representation, we performed ab initio molecular dynamics simulations to prepare and equilibrate the catalyst model. This allowed the critical capture of the dynamicity of Ag and ZrO_2 on the SiO_2 support and its susceptibility to arrangement under different operating conditions. The quenched ground state at the end of the AIMD simulation was used as a starting point to determine the reaction energies. AIMD simulations were performed within the canonical ensemble using a Nosé−Hoover chain thermostat and a time step of 1 fs. The $Ag\text{-}ZrO_2/SiO_2$ catalyst model was initially heated to 1800 K, followed by multiple canonical ensemble simulations with systematic temperature ramp down every 200 K (1800, 1600, 1400, 1200, and 1000 K). The simulated annealing procedures provided a systematic method to allow temperature-stimulated simultaneous rearrangement of the SiO_2 support (amorphization) and Ag dispersion. Simulation trajectories were collected for 2 to 3 ps at every temperature hold. This was followed by a microcanonical ensemble annealing simulation, where the system was allowed to cool from 1000 to 0 K using a time step of 1 fs and a rescaling factor of 0.9995 for annealing velocities. Data collected for analysis used a total simulation run time of 20 ps at the end of the annealing algorithm. A comprehensive description of the catalyst model was provided in our previous study that investigated the impact of Ag dispersion in the $Ag\text{-}ZrO_2/SiO_2$ catalyst on the reaction selectivity of ethanol conversion to 1,3-butadiene and ethylene.[37] To simulate the $Ag\text{-}ZrO_2/SiO_2$ catalyst in the presence of H_2, H_2 molecules were introduced into the simulation box containing the dispersed $Ag\text{-}ZrO_2/SiO_2$ catalyst model. A canonical ensemble simulation was conducted for 3.5 ps at 600 K and then cooled to 0 K using microcanonical ensemble simulation annealing. A time step of 1 fs and rescaling factor of 0.9995 was used for the annealing velocities. Figure S2 provides illustrations of the optimized $Ag\text{-}ZrO_2/SiO_2$ catalyst at the end of the AIMD runs simulated in the absence (Figure S2a) and presence of H_2 (Figure S2b).

The thermodynamic free energies ($\Delta G_{298\ K}$ in eV) for the $Ag/ZrO_2/SiO_2$ catalysts in the absence and presence of adsorbed H_2 were calculated using energies obtained from DFT calculations (E_{DFT}), corrected to include the effect of zero-point vibrational energy, entropy, and enthalpy corrections. The vibrational corrections were derived from harmonic vibrational frequency calculations, while the entropic corrections employed statistical mechanic relations at standard temperature and pressure. The predicted adsorption and surface-mediated reaction phenomenon is critically linked to the available active sites in the catalyst and hence is sensitive to the catalyst build and the binding mode of the intermediates. To evaluate the susceptibility of the binding modes of reaction intermediates to the build of the simulated catalyst model, we previously conducted a systematic evaluation of the interaction energies between adsorbates and the catalyst model.[37] The binding energies were computed as a function of supported Ag (SiO_2 support), unsupported planar Ag (111), and in the presence and absence of ZrO_2 to decouple the multi-

https://dx.doi.org/10.1021/acscatal.0c02235
ACS Catal. 2020, 10, 10602−10613

functionality and activity contribution from different surface sites in the $Ag/ZrO_2/SiO_2$ model. The resulting optimized adsorbate configurations considered here and in our previous study[37] were selected based on the results of a detailed assessment of binding energy trends to investigate the mode of interaction and the relative alignment of the adsorbate molecule to the catalyst surface.

■ ASSOCIATED CONTENT

Supporting Information

The Supporting Information is available free of charge at https://pubs.acs.org/doi/10.1021/acscatal.0c02235.

Computational model details, atomic density distribution of species in $Ag\text{-}ZrO_2/SiO_2$ catalysts models, effect of adsorbed hydrogen on the distribution and oxidation state of Ag in $Ag\text{-}ZrO_2/SiO_2$ catalyst models, visual representation of key selectivity determining reaction intermediates on the $Ag\text{-}ZrO_2/SiO_2$ (H_2-free) catalyst surface in the absence of adsorbed hydrogen, visual representation of key selectivity determining reaction intermediates on the $Ag\text{-}ZrO_2/SiO_2$ catalyst surface in the presence of adsorbed hydrogen, X-ray diffraction, transmission electron microscopy (PDF)

■ AUTHOR INFORMATION

Corresponding Authors

Vanessa Lebarbier Dagle − *Pacific Northwest National Laboratory, Richland, Washington 99352, United States;* orcid.org/0000-0003-4943-9455; Email: vanessa.dagle@pnnl.gov

Robert A. Dagle − *Pacific Northwest National Laboratory, Richland, Washington 99352, United States;* Email: robert.dagle@pnnl.gov

Authors

Austin D. Winkelman − *Pacific Northwest National Laboratory, Richland, Washington 99352, United States; Voiland School of Chemical Engineering and Bioengineering, Washington State University, Pullman, Washington 99164, United States*

Nicholas R. Jaegers − *Pacific Northwest National Laboratory, Richland, Washington 99352, United States; Voiland School of Chemical Engineering and Bioengineering, Washington State University, Pullman, Washington 99164, United States;* orcid.org/0000-0002-9930-7672

Johnny Saavedra-Lopez − *Pacific Northwest National Laboratory, Richland, Washington 99352, United States*

Jianzhi Hu − *Pacific Northwest National Laboratory, Richland, Washington 99352, United States;* orcid.org/0000-0001-8879-747X

Mark H. Engelhard − *Environmental Molecular Sciences Laboratory, Pacific Northwest National Laboratory, Richland, Washington 99352, United States;* orcid.org/0000-0002-5543-0812

Susan E. Habas − *National Bioenergy Center, National Renewable Energy Laboratory, Golden, Colorado 80401, United States;* orcid.org/0000-0002-3893-8454

Sneha A. Akhade − *Pacific Northwest National Laboratory, Richland, Washington 99352, United States; Materials Sciences Division, Lawrence Livermore National Laboratory, Livermore, California 94550, United States;* orcid.org/0000-0003-0024-2299

Libor Kovarik − *Pacific Northwest National Laboratory, Richland, Washington 99352, United States*

Vassilliki-Alexandra Glezakou − *Pacific Northwest National Laboratory, Richland, Washington 99352, United States;* orcid.org/0000-0001-6028-7021

Roger Rousseau − *Pacific Northwest National Laboratory, Richland, Washington 99352, United States;* orcid.org/0000-0003-1947-0478

Yong Wang − *Pacific Northwest National Laboratory, Richland, Washington 99352, United States; Voiland School of Chemical Engineering and Bioengineering, Washington State University, Pullman, Washington 99164, United States;* orcid.org/0000-0002-8460-7410

Complete contact information is available at: https://pubs.acs.org/10.1021/acscatal.0c02235

Notes

The authors declare no competing financial interest.

■ ACKNOWLEDGMENTS

This work was financially supported by the U.S. Department of Energy (DOE), Office of Energy Efficiency and Renewable Energy, Bioenergy Technologies Office, and was performed at the Pacific Northwest National Laboratory (PNNL) under Contract No. DE-AC05-76RL01830 and the National Renewable Energy Laboratory under Contract No. DE-AC36-08GO28308. Part of the work conducted by S. A. Akhade was performed under the auspices of the U.S. DOE at Lawrence Livermore National Laboratory under Contract No. DE-AC52-07NA27344. This work was partly supported through the PNNL-WSU Distinguished Graduate Research Program for ADW. NMR and XPS experiments were performed using EMSL (grid.436923.9), a DOE Office of Science User Facility sponsored by the Office of Biological and Environmental Research. The views and opinions of the authors expressed herein do not necessarily state or reflect those of the U.S. Government or any agency thereof. Neither the U.S. Government nor any agency thereof, nor any of their employees, makes any warranty, expressed or implied, or assumes any legal liability or responsibility for the accuracy, completeness, or usefulness of any information, apparatus, product, or process disclosed, or represents that its use would not infringe privately owned rights.

■ REFERENCES

(1) Badger, P. C. Ethanol from cellulose: a general review. In *Trends in New Crops and New Uses;* Janick, J., Whipkey, A., Eds.; ASHS Press: Alexandria, VA, 2002; pp 17−21.

(2) Roy, P.; Dutta, A. A review of life cycle of ethanol produced from biosyngas. *Bioethanol* **2013**, *1* (1), 9−19.

(3) Luk, H. T.; Mondelli, C.; Curulla Ferré, D.; Stewart, J. A.; Perez-Ramirez, J. Status and prospects in higher alcohols synthesis from syngas. *Chem. Soc. Rev.* **2017**, *46*, 1358−1426.

(4) Chen, Y.; Zhang, H.; Ma, H.; Qian, W.; Jin, F.; Ying, W. Direct Conversion of Syngas to Ethanol over Rh−Fe/γ-Al2O3 Catalyst: Promotion Effect of Li. *Catal. Lett.* **2018**, *148* (2), 691−698.

(5) Abubackar, H. N.; Veiga, M. C.; Kennes, C. Carbon monoxide fermentation to ethanol by Clostridium autoethanogenum in a bioreactor with no accumulation of acetic acid. *Bioresour. Technol.* **2015**, *186*, 122−127.

(6) Rajagopalan, S.; Datar, R. P.; Lewis, R. S. Formation of ethanol from carbon monoxide via a new microbial catalyst. *Biomass Bioenergy* **2002**, *23*, 487−493.

(7) Eagan, N.; Kumbhalkar, M. D.; Buchanan, J. S.; Dumesic, J. A.; Huber, G. W. Chemistries and processes for the conversion of ethanol into middle-distillate fuels. *Nature Reviews Chemistry* **2019**, *3*, 223−249.
(8) Sun, J.; Wang, Y. Recent Advances in Catalytic Conversion of Ethanol to Chemicals. *ACS Catal.* **2014**, *4* (4), 1078−1090.
(9) Baylon, R. A. L.; Sun, J.; Martin, K. J.; Venkitasubramanian, P.; Wang, Y. Beyond ketonization: selective conversion of carboxylic acids to olefins over balanced Lewis acid−base pairs. *Chem. Commun.* **2016**, *52* (28), 4975−4978.
(10) Andrei, R. D.; Popa, M. I.; Fajula, F.; Hulea, V. Heterogeneous oligomerization of ethylene over highly active and stable Ni-AlSBA-15 mesoporous catalysts. *J. Catal.* **2015**, *323*, 76−84.
(11) Lilga, M. A.; Hallen, R. T.; Albrecht, K. O.; Cooper, A. R.; Frye, J. G.; Ramasamy, K. K. Systems and processes for conversion of ethylene feedstocks to hydrocarbon fuels. US9,663,416, 2017.
(12) Saavedra Lopez, J.; Dagle, R. A.; Dagle, V. L.; Smith, C.; Albrecht, K. O. Oligomerization of ethanol-derived propene and isobutene mixtures to transportation fuels: catalyst and process considerations. *Catal. Sci. Technol.* **2019**, *9* (5), 1117−1131.
(13) Galadima, A.; Muraza, O. Zeolite catalysts in upgrading of bioethanol to fuels range hydrocarbons: A review. *J. Ind. Eng. Chem.* **2015**, *31*, 1−14.
(14) Ferreira Madeira, F.; Ben Tayeb, K.; Pinard, L.; Vezin, H.; Maury, S.; Cadran, N. Ethanol transformation into hydrocarbons on ZSM-5 zeolites: Influence of Si/Al ratio on catalytic performances and deactivation rate. Study of the radical species role. *Appl. Catal., A* **2012**, *443*−*444*, 171−180.
(15) Müller, P.; Wang, S.-C.; Burt, S. P.; Hermans, I. Influence of Metal Doping on the Lewis Acid Catalyzed Production of Butadiene from Ethanol Studied by using Modulated Operando Diffuse Reflectance Infrared Fourier Transform Spectroscopy and Mass Spectrometry. *ChemCatChem* **2017**, *9* (18), 3572−3582.
(16) Blay, V.; Epelde, E.; Miravalles, R.; Perea, L. A. Converting olefins to propene: Ethene to propene and olefin cracking. *Catal. Rev.: Sci. Eng.* **2018**, *60* (2), 278−335.
(17) Sun, J.; Zhu, K.; Gao, F.; Wang, C.; Liu, J.; Peden, C. H. F.; Wang, Y. Direct Conversion of Bio-ethanol to Isobutene on Nanosized ZnxZryOz Mixed Oxides with Balanced Acid−Base Sites. *J. Am. Chem. Soc.* **2011**, *133* (29), 11096−11099.
(18) Smith, C.; Dagle, V. L.; Flake, M.; Ramasamy, K. K.; Kovarik, L.; Bowden, M.; Onfroy, T.; Dagle, R. A. Conversion of syngas-derived C2+ mixed oxygenates to C3−C5 olefins over ZnxZryOz mixed oxide catalysts. *Catal. Sci. Technol.* **2016**, *6* (7), 2325−2336.
(19) Dagle, V. L.; Smith, C.; Flake, M.; Albrecht, K. O.; Gray, M. J.; Ramasamy, K. K.; Dagle, R. A. Integrated process for the catalytic conversion of biomass-derived syngas into transportation fuels. *Green Chem.* **2016**, *18* (7), 1880−1891.
(20) Dagle, V. L.; Flake, M. D.; Lemmon, T. L.; Lopez, J. S.; Kovarik, L.; Dagle, R. A. Effect of the SiO2 support on the catalytic performance of Ag/ZrO2/SiO2 catalysts for the single-bed production of butadiene from ethanol. *Appl. Catal., B* **2018**, *236*, 576−587.
(21) Sushkevich, V. L.; Ivanova, I. I.; Tolborg, S.; Taarning, E. Meerwein−Ponndorf−Verley−Oppenauer reaction of crotonaldehyde with ethanol over Zr-containing catalysts. *J. Catal.* **2014**, *316*, 121−129.
(22) Fischer, L.; Hausen, M. Z.; Wember, K. Process for the continuous manufacture of n-butyraldehyde by selective hydrogenation of crotonaldehyde in the liquid phase in the presence of palladium-aluminum oxide catalyst. US4,450,300, 1984.
(23) Makshina, E. V.; Dusselier, M.; Janssens, W.; Degreve, J.; Jacobs, P. A.; Sels, B. F. Review of old chemistry and new catalytic advances in the on-purpose synthesis of butadiene. *Chem. Soc. Rev.* **2014**, *43* (22), 7917−7953.
(24) Ning, X.; Xu, Y.-M.; Wu, A.-Q.; Tang, C.; Jia, A.-P.; Luo, M.-F.; Lu, J.-Q. Kinetic study of selective hydrogenation of crotonaldehyde over Fe-promoted Ir/BN catalysts. *Appl. Surf. Sci.* **2019**, *463*, 463−473.
(25) Taniya, K.; Yu, C. H.; Takado, H.; Hara, T.; Okemoto, A.; Horie, T.; Ichihashi, Y.; Tsang, S. C.; Nishiyama, S. Synthesis of bimetallic SnPt-nanoparticle catalysts for chemoselective hydrogenation of crotonaldehyde: Relationship between SnxPty alloy phase and catalytic performance. *Catal. Today* **2018**, *303*, 241−248.
(26) Quattlebaum, W. M.; Toussaint, W. J.; Dunn, J. T. Deoxygenation of certain aldehydes and ketones - preparation of butadiene and styrene. *J. Am. Chem. Soc.* **1947**, *69*, 593.
(27) Gunst, D.; Alexopoulos, K.; Van Der Borght, K.; John, M.; Galvita, V.; Reyniers, M.-F.; Verberckmoes, A. Study of butanol conversion to butenes over H-ZSM-5: Effect of chemical structure on activity, selectivity and reaction pathways. *Appl. Catal., A* **2017**, *539*, 1−12.
(28) Jaegers, N. R.; Wang, Y.; Hu, J. Z. Thermal perturbation of NMR properties in small polar and non-polar molecules. *Sci. Rep.* **2020**, *10* (1), 6097.
(29) Phung, T. K.; Proietti Hernandez, L.; Busca, G. Conversion of Ethanol Over Transition Metal Oxide Catalysts: Effect of Tungsta Addition on Catalytic Behavior Of Titania and Zirconia. *Appl. Catal., A* **2015**, *489*, 180−187, DOI: 10.1016/j.apcata.2014.10.025.
(30) Humbird, D.; Davis, R.; Tao, L.; Kinchin, C.; Hsu, D.; Aden, A.; Schoen, P.; Lukas, J.; Olthof, B.; Worley, M.; Sexton, D.; Dudgeon, D. *Process Design and Economics for Biochemical Conversion of Lignocellulosic Biomass to Ethanol;* National Renewable Energy Laboratory, 2011.
(31) Parry, E. P. An infrared study of pyridine adsorbed on acidic solids. Characterization of surface acidity. *J. Catal.* **1963**, *2* (5), 371−379.
(32) Miyata, H.; Tokuda, S.; Ono, T.; Ohno, T.; Hatayama, F. Infrared, laser-Raman and X-ray diffraction investigation of MoO3/ZrO2 and the oxidation of (Z)-but-2-ene. *J. Chem. Soc., Faraday Trans.* **1990**, *86* (12), 2291−2295.
(33) Kondo, J. N.; Nishitani, R.; Yoda, E.; Yokoi, T.; Tatsumi, T.; Domen, K. A comparative IR characterization of acidic sites on HY zeolite by pyridine and CO probes with silica−alumina and γ-alumina references. *Phys. Chem. Chem. Phys.* **2010**, *12* (37), 11576−11586.
(34) Xu, W.; Miller, S. J.; Agrawal, P. K.; Jones, C. W. Positive Effect of Water on Zeolite BEA Catalyzed Alkylation of Phenol with Propylene. *Catal. Lett.* **2014**, *144* (3), 434−438.
(35) Ward, J. W. The nature of active sites on zeolites: IV. The influence of water on the acidity of X and Y type zeolites. *J. Catal.* **1968**, *11* (3), 238−250.
(36) West, R. M.; Braden, D. J.; Dumesic, J. A. Dehydration of butanol to butene over solid acid catalysts in high water environments. *J. Catal.* **2009**, *262* (1), 134−143.
(37) Akhade, S. A.; Winkelman, A.; Lebarbier Dagle, V.; Kovarik, L.; Yuk, S. F.; Lee, M.-S.; Zhang, J.; Padmaperuma, A. B.; Dagle, R. A.; Glezakou, V.-A.; Wang, Y.; Rousseau, R. Influence of Ag metal dispersion on the thermal conversion of ethanol to butadiene over Ag-ZrO2/SiO2 catalysts. *J. Catal.* **2020**, *386*, 30−38.
(38) Mizuno, S.; Kurosawa, M.; Tanaka, M.; Iwamoto, M. One-path and Selective Conversion of Ethanol to Propene on Scandium-modified Indium Oxide Catalysts. *Chem. Lett.* **2012**, *41* (9), 892−894.
(39) Bi, J.; Liu, M.; Song, C.; Wang, X.; Guo, X. C2−C4 light olefins from bioethanol catalyzed by Ce-modified nanocrystalline HZSM-5 zeolite catalysts. *Appl. Catal., B* **2011**, *107* (1), 68−76.
(40) Inaba, M.; Murata, K.; Saito, M.; Takahara, I. Production of olefins from ethanol by Fe-supported zeolite catalysts. *Green Chem.* **2007**, *9* (6), 638−646.
(41) Gayubo, A. G.; Alonso, A.; Valle, B.; Aguayo, A. T.; Olazar, M.; Bilbao, J. Hydrothermal stability of HZSM-5 catalysts modified with Ni for the transformation of bioethanol into hydrocarbons. *Fuel* **2010**, *89* (11), 3365−3372.
(42) Iwamoto, M.; Kasai, K.; Haishi, T. Conversion of Ethanol into Polyolefin Building Blocks: Reaction Pathways on Nickel Ion-loaded Mesoporous Silica. *ChemSusChem* **2011**, *4*, 1055−1058.
(43) Iwamoto, M. Selective catalytic conversion of bio-ethanol to propene: A review of catalysts and reaction pathways. *Catal. Today* **2015**, *242*, 243−248.

(44) Perdew, J. P.; Burke, K.; Ernzerhof, M. Generalized Gradient Approximation Made Simple. *Phys. Rev. Lett.* **1996**, *77* (18), 3865−3868.
(45) VandeVondele, J.; Krack, M.; Mohamed, F.; Parrinello, M.; Chassaing, T.; Hutter, J. Quickstep: Fast and accurate density functional calculations using a mixed Gaussian and plane waves approach. *Comput. Phys. Commun.* **2005**, *167*, 103−128.
(46) Goedecker, S.; Teter, M.; Hutter, J. Separable dual-space Gaussian pseudopotentials. *Phys. Rev. B: Condens. Matter Mater. Phys.* **1996**, *54*, 1703−1710.
(47) VandeVondele, J.; Hutter, J. Gaussian Basis Sets for Accurate Calculations on Molecular Systems in Gas and Condensed Phases. *J. Chem. Phys.* **2007**, *127*, 114105.
(48) Grimme, S. Semiempirical GGA-type density functional constructed with a long-range dispersion correction. *J. Comput. Chem.* **2006**, *27*, 1787−1799.

https://dx.doi.org/10.1021/acscatal.0c02235
ACS Catal. 2020, 10, 10602−10613